ADVANCED SUSTAINABLE SYSTEMS
www.advsustainsys.com

Degradation of Tetracycline by Fe-N-Coordinated Porous Carbon Activated PMS: High Dispersibility and Stability

Shenghui Wang, Yanhua Song, Yansong Wu, Bin Wang, Xue Gao, Xingwang Zhu, Jinyuan Liu,* and Paul K. Chu**

Advanced oxidation processes (AOPs) leverage the generation of reactive radicals or non-radical species, which exhibit strong oxidative potential, to effectively degrade recalcitrant pollutants. Herein, Fe_5-NG is synthesized by a one-step calcination method for the degradation of tetracycline (TC). A large nitrogen concentration enhances the activation ability of Fe_5-NG toward PMS, as manifested by 100% degradation of TC within 12 min for TC concentrations below 25 mg L^{-1} under visible light irradiation. The Fe_5-NG/PMS system degrades TC via the generation of $SO_4^{\bullet-}$ and $^1O_2$, and the presence of Fe(IV) = O species is confirmed. X-ray photoelectron spectroscopy performed on Fe_5-NG before and after the treatment shows that pyridine nitrogen and graphite nitrogen are the primary active nitrogen species responsible for PMS activation, and PMS accelerates the Fe(III)/Fe(II) redox cycle by forming abundant active nitrogen species. The underlying degradation mechanism of the Fe_5-NG/PMS system is investigated, and the non-free radical ($^1O_2$) pathway is dominant.

1. Introduction

Environmental pollutants, especially antibiotics like tetracycline (TC), pose serious risks to health and ecosystems. Traditional remediation methods are often costly, time-consuming, and inherently limited in efficiency (e.g., incomplete degradation, secondary pollution)[1,2] To address these challenges, advanced photocatalytic oxidation systems have emerged as a promising alternative due to their high reactivity and environmental compatibility.[3] Photocatalysis, a technique that utilizes light energy to activate catalysts, expedites the degradation of organic and inorganic pollutants. It can also be combined with advanced oxidation processes (AOPs) to produce reactive species, including singlet oxygen ($^1O_2$), superoxide radicals ($O_2^{\bullet-}$), and hydroxyl radicals ($^\bullet$OH), to accelerate the oxidative degradation of organic compounds.[4,5] Photocatalysis is an integral part of the advanced oxidation technology, which includes ozone oxidation,[2,6] Fenton reactions,[7,8] and ultrasonic oxidation.[9] AOPs are used for water and air purification due to low cost, sustainability, and minimally harmful by-products. Photocatalysis and AOPs offer an innovative approach to environmental remediation that can mitigate pollution.[10]

Among the various types of catalytic materials, carbon materials are known for their high catalytic activity, uniform distribution, and cost-effectiveness.[11] Carbonaceous include carbon nanotubes,[12] carbonized polymer dots,[13] biochar,[14] and carbon quantum dots,[15–17] which can be synthesized by various methods such as pyrolysis,[18] chemical vapor deposition,[19] solvothermal methods,[20] and templating techniques.[21] The synthesis temperature and method affect the structure and properties of the materials. For instance, pyrolysis typically occurs in the temperature range between 500 and 1000 °C to enhance the crystallinity,[22] increase the aggregation of active sites,[23] and improve the adsorption capacity. There are several kinds of precursors for the reactions, including organic polymers,[24] natural materials,[14,25] organic metal complexes,[26] carbonaceous compounds,[27] and vapor deposition materials. These precursors, which can be converted into various forms of carbon materials under different synthesis conditions, impact the structure and catalytic properties of the products.

Pure carbon materials have limitations in certain applications and require doping to enhance their performance. Metal doping has been shown to improve the electrochemical properties and catalytic activity.[28] For example, doping with iron,[29]

S. Wang, Y. Song, Y. Wu
School of Environmental and Chemical Engineering
Jiangsu University of Science and Technology
Zhenjiang, Jiangsu 212003, P. R. China
E-mail: songyh@just.edu.cn

B. Wang, J. Liu, P. K. Chu
Department of Physics, Department of Materials Science and Engineering, and Department of Biomedical Engineering
City University of Hong Kong
Tat Chee Avenue, Kowloon, Hong Kong 999077, P. R. China
E-mail: jyliu@ujs.edu.cn; paul.chu@cityu.edu.hk

X. Gao, J. Liu
Institute for Energy Research, School of the Environment and Safety Engineering
Jiangsu University
Zhenjiang, Jiangsu 212013, P. R. China

X. Zhu
Institute of Technology for Carbon Neutralization, College of Environmental Science and Engineering
Yangzhou University
Yangzhou 225009, P. R. China

The ORCID identification number(s) for the author(s) of this article can be found under https://doi.org/10.1002/adsu.202500219

DOI: 10.1002/adsu.202500219

cobalt,[30,31] and nickel[32] increases the conductivity and number of active sites. In particular, Fe doping is attractive on account of the abundant resource, low cost, and ability to enhance the oxygen reduction reaction.[33] Iron doping promotes electron transfer within the catalyst. Meanwhile, heteroatom doping (e.g., nitrogen,[34] sulfur,[35] or phosphorus)[36] further enhances catalytic activity by modifying the electronic structure and increasing the density of active sites. N doping is preferred over doping with other heteroatoms because it can alter the electronic structure of carbon materials, increase the number of active sites, and improve the catalytic properties.[39] Advances in Fe-N coordinated catalysts have demonstrated that atomic-level dispersion of Fe can be achieved through controlled pyrolysis of metal-organic precursors.[37] For instance, Guo et al.[38] revealed that stabilizing Fe single atoms by using the nitrogen sites of pyridine as anchor points can prevent metal agglomeration and enhance the stability of the catalyst. Moreover, nitrogen can improve the conductivity and stability of carbon materials. In order to optimize the process, the proper precursor is crucial. By using organic metal complexes as precursors, carbon materials with a large surface area and porous structure can be synthesized by pyrolysis, and metal doping can be accomplished during the carbonization process.[40]

Metal phthalocyanine (MPc),[41] an organometallic complex with a unique electronic structure and high design flexibility, is a promising precursor. By modifying the metal ions, peripheral ligands, and axial ligands, diverse functions can be obtained. Iron phthalocyanine (FePc) is an iron-containing phthalocyanine compound with an iron atom in the center of the molecular structure.[42] Similar to porphyrin,[43] owing to the large molecular structure of phthalocyanine, the iron atoms are coordinated in the center,[44] thereby solving the problem of metal agglomeration when iron salts are used in traditional synthesis.[45] The metal atoms act as the active sites in the catalytic reaction due to their high surface activity. The dispersed atoms are more likely to come into contact with reactants to increase the reaction rate,[29,46] and the electronic structure of the dispersed metal atoms can be finely tuned by adjusting the coordination environment. Consequently, atomic utilization is higher, and the catalytic efficiency is better. At the same time, phthalocyanine also serves as a carbon source to reduce the complexity of the synthesis.[47,48]

Herein, Fe_5-NG porous carbon is prepared by one-step calcination, and tetracycline (TC) is the target pollutant to assess the performance of the catalyst by the PMS method. Electron spin resonance (ESR) and capture experiments reveal that the primary active species. The Fe(III)/Fe(II) redox cycle is studied, and the catalytic degradation mechanism and pathways[49] are discussed. The results reveal not only an effective strategy to address the activation energy deficiency of the Fe(III)/PMS system but also the immense potential for environmental remediation.

2. Experimental Section

2.1. Chemicals and Reagents

The reagents used in this study, including iron phthalocyanine (FePc, $(C_8H_4N_2)_4Fe$), potassium peroxymonosulfate (PMS), anhydrous ethanol, tetracycline, sodium bicarbonate, methanol (MeOH), humic acid (HA), sodium carbonate, tert-butanol (TBA), potassium bromide, and furfuryl alcohol (FFA), were purchased from Shanghai Macklin Biochemical Co., Ltd. Urea, benzoquinone (BQ), dimethyl sulfoxide (DMSO), sodium chloride, and anhydrous trisodium phosphate were obtained from Sinopharm Chemical Reagent Co., Ltd. All the reagents were analytical grade and used without further purification. The TOC and COD of lake water and tap water in the experiment were TOC_L = 7.78 mg L^{-1}, TOC_T = 1.03 mg L^{-1}, COD_L = 5.36 mg L^{-1}, and COD_T = 1.41 mg L^{-1} respectively. Deionized water (resistivity of 18.25 MΩcm^{-1}) was used in the experiments.

2.2. Preparation of Photocatalytic Materials

Fe_5-NG was prepared as shown in **Scheme 1**. First, 10 g urea and 0.5 g FePc were pulverized using a mortar, transferred to a tube furnace, and calcined at 600 °C (3 °C min^{-1}) under N_2 for 2 h. After the tube furnace cooled to ambient temperature, the black powdery product was gathered. Fe_x-NG samples ($Fe_{0.5}$-NG, Fe_1-NG, Fe_5-NG, and Fe_{10}-NG) with different Fe concentrations were prepared by adjusting the ratios of urea and FePc, where x refers to the mass ratio of added FePc to urea (0.5%, 1%, 5%, and 10%, respectively). For comparison, a conventional Fe-doped g-C_3N_4 catalyst (Fe-CN) with the same molar amount of Fe was prepared using $Fe(NO_3)_3{\cdot}9H_2O$ (355.4 mg) as the iron precursor. Additionally, g-C_3N_4(CN) and N-modified porous carbon (NG) were prepared by calcining urea and a mixture of urea and phthalocyanine, respectively.

2.3. Characterization

The crystallinity and phase composition of the powder were analyzed by X-ray diffraction (XRD) with Cu K_α radiation on a Bruker D8 diffractometer. Fourier transform infrared (FT-IR) spectroscopy was conducted using the potassium bromide wafer technique on a Bruker VERTEX-70 spectrometer. The morphology was examined by scanning electron microscopy (SEM, model JSM-7800F) and transmission electron microscopy (TEM, model JEM-2100). The specific surface areas and pore size distributions were measured by the Brunauer-Emmett-Teller (BET) method utilizing nitrogen adsorption/desorption monitored on the ASAP2010 V5. The surface chemistry and chemical states of the catalysts were determined by X-ray photoelectron spectroscopy (XPS) on the Shimadzu AXIS, and electron spin resonance (ESR) spectroscopy (JES-FA200) was employed to identify the different reactive radicals.

2.4. Catalytic Degradation

Fe_5-NG (10 mg) was added to a beaker containing 100 mL of the tetracycline solution with a specific concentration and kept at approximately 25 °C. The pH was regulated by adding H_2SO_4 and NaOH, and 4 mL were withdrawn with a syringe every 2 minutes for 12 minutes. Each sample was mixed with 0.5 mL of methanol and shaken to quench the radicals and terminate the degradation process. The solution was passed through a 0.22 μm filter and placed in a quartz cuvette. The absorbance of TC at 356 nm was measured by UV–vis spectrophotometry (Hitach-3010) to determine the degree of degradation. The reusability was assessed by

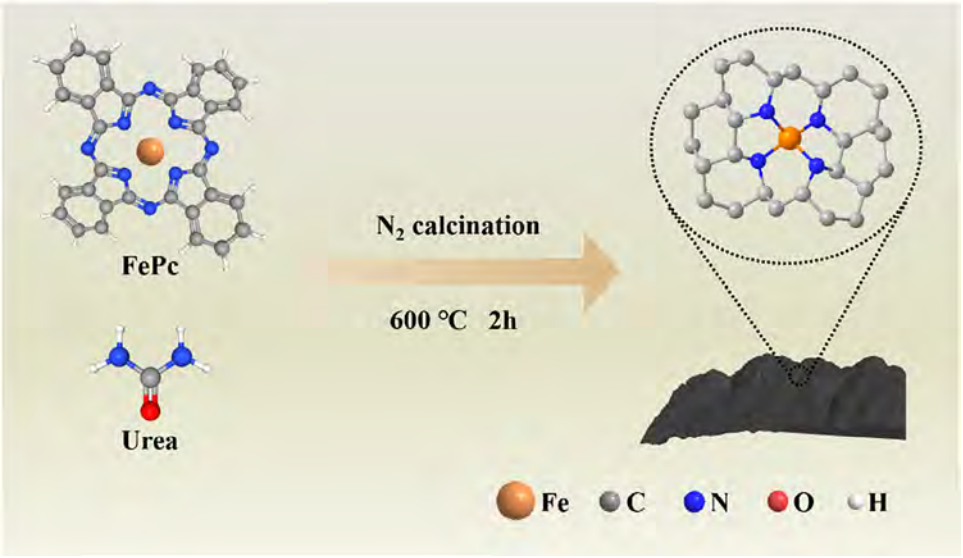

Scheme 1. Schematic of the synthesis of Fe-NG.

centrifugation after degradation, washing several times successively with deionized water and ethanol, and drying at 60 °C. The dried catalyst was then used for the next round of experiments.

3. Results and Discussion

3.1. Structure and Morphology

The XRD spectra of the four samples are presented in **Figure 1a**. The (100) planes of CN and Fe-CN correspond to the in-plane repeating units of the heptazine rings in carbon nitride, while the (002) plane represents the interlayer stacking of carbon nitride.[50] These peaks are characteristic of g-C_3N_4. In comparison, the intensity of the (002) plane of g-C_3N_4 of NG and Fe_5-NG diminishes, likely because the incorporation of FePc reduces the crystallinity of g-C_3N_4. At the same time, the pyrolysis of phthalocyanine may introduce additional defects, disrupting the ordered structure of graphite and resulting in a looser interlayer configuration along with the formation of a porous architecture. This alteration leads to an expansion of the interlayer spacing and a weakening of interlayer bonding forces, thereby inducing a leftward shift in the (002) plane.[48,51] Interestingly, no Fe species are observed from the Fe_5-NG samples, indicating that there are no Fe crystalline species, and Fe atoms are highly dispersed.

Figure 1 shows the FTIR spectra. The peak at 812 cm^{-1} of CN and Fe-CN stems from triazine, and the broad peaks between 900 and 1800 cm^{-1} are C-N and C = N tensile vibrations characteristic of g-C_3N_4. The broad peaks between 3000 and 3500 cm^{-1} represent N-H vibration or adsorbed H_2O.[53,54] The typical peaks of g-C_3N_4 of NG and Fe_5-NG become blurred as FePc introduced

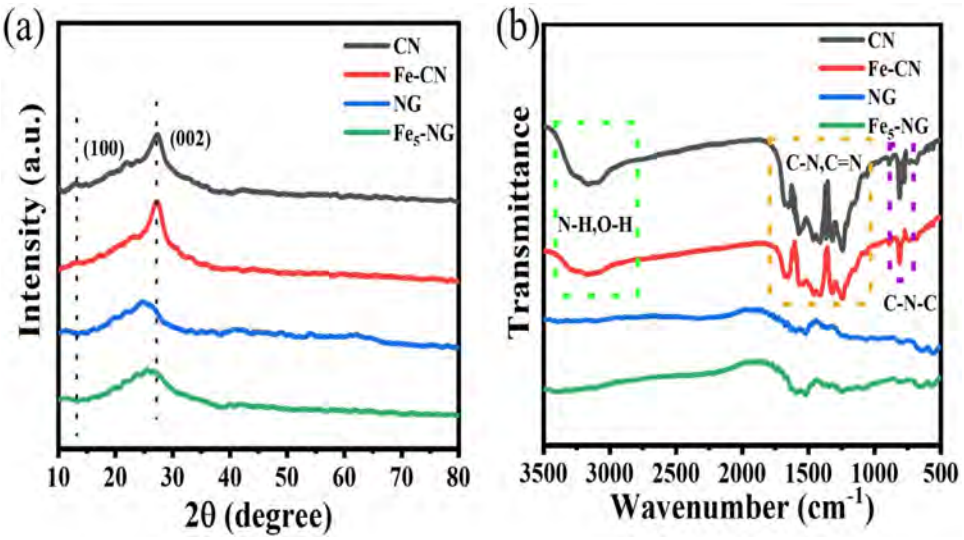

Figure 1. a) XRD and b) FTIR spectra of the four samples.

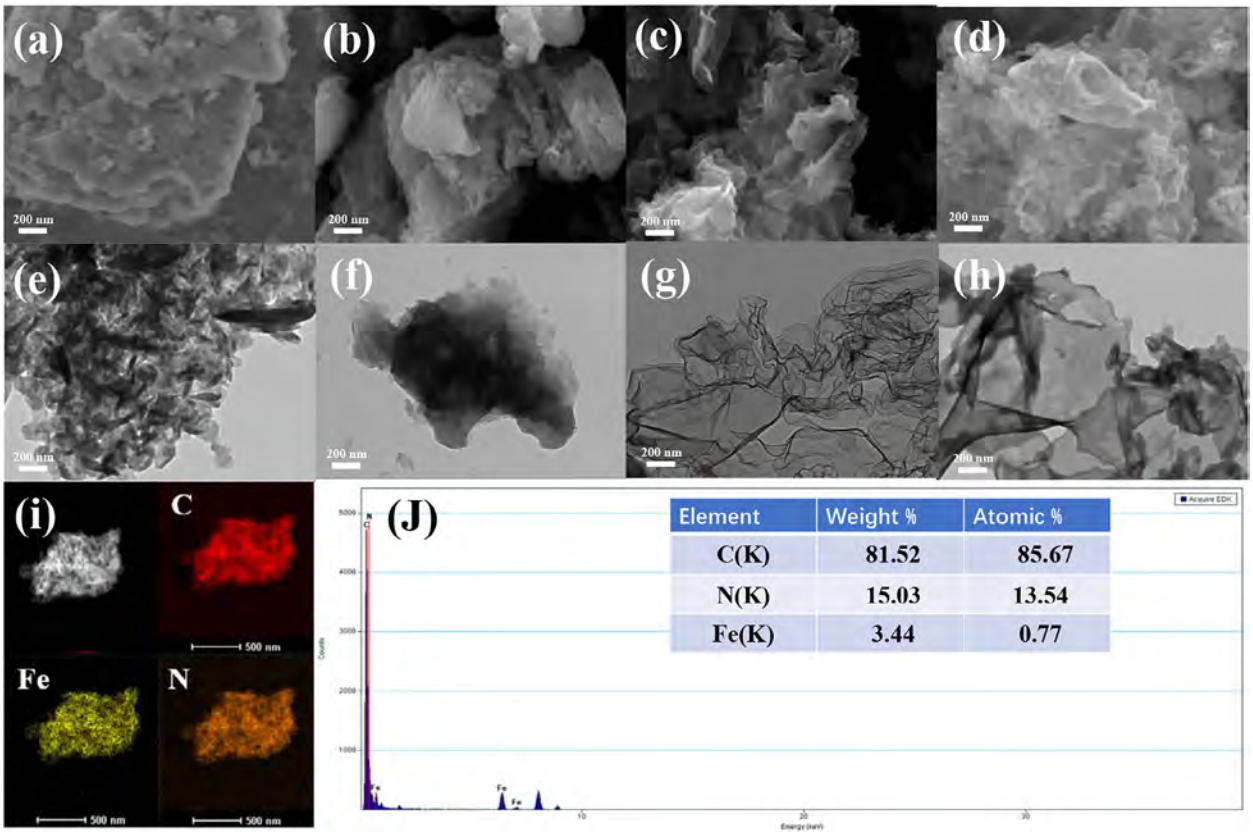

Figure 2. SEM images of a) CN, b) Fe-CN, c) NG, d) Fe_5-NG; TEM images of e) CN, f) Fe-CN, g) NG, h) Fe_5-NG; i) Elemental maps of C, N, and Fe in Fe_5-NG; j) EDS spectrum of Fe_5-NG.

during pyrolysis curbs the thermal condensation of urea to form a unique carbon matrix.[55]

Figure 2 shows the morphology of CN, Fe-CN, NG, and Fe_5-NG by SEM and TEM. The unmodified CN has a bulk structure (Figure 2a) and Fe-CN after Fe doping has a particle-stacked structure (Figure 2b), which is confirmed by the TEM image in Figure 2f. The structure is changed by incorporating phthalocyanine, and gases such as H_2O, CO, and CO_2 formed during pyrolysis[56] create the porous structure and strip the carbon nanosheets to form layered structures in NG and Fe_5-NG (Figure 2c,d and g,h). The EDS elemental maps of C, N, and Fe of Fe_5-NG are presented in Figure 2i,j confirms Fe doping.

The pore size and specific surface area are derived from the N_2 adsorption-desorption isotherms (**Figure 3**), which reveal that Fe-CN and Fe_5-NG are type IV with H3 hysteresis loops, indicative of a mesoporous structure. The hysteresis of Fe_5-NG shifts

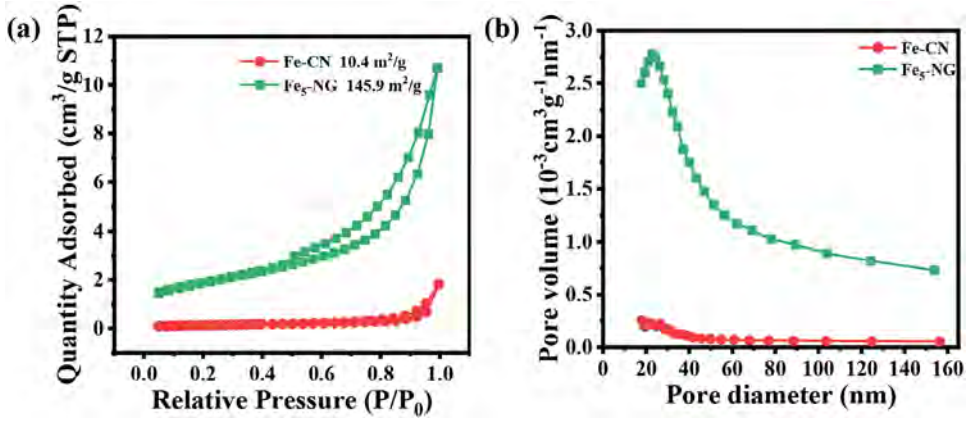

Figure 3. a) N_2 adsorption-desorption isotherms and b) BJH pore size distribution of Fe-CN and Fe_5-NG.

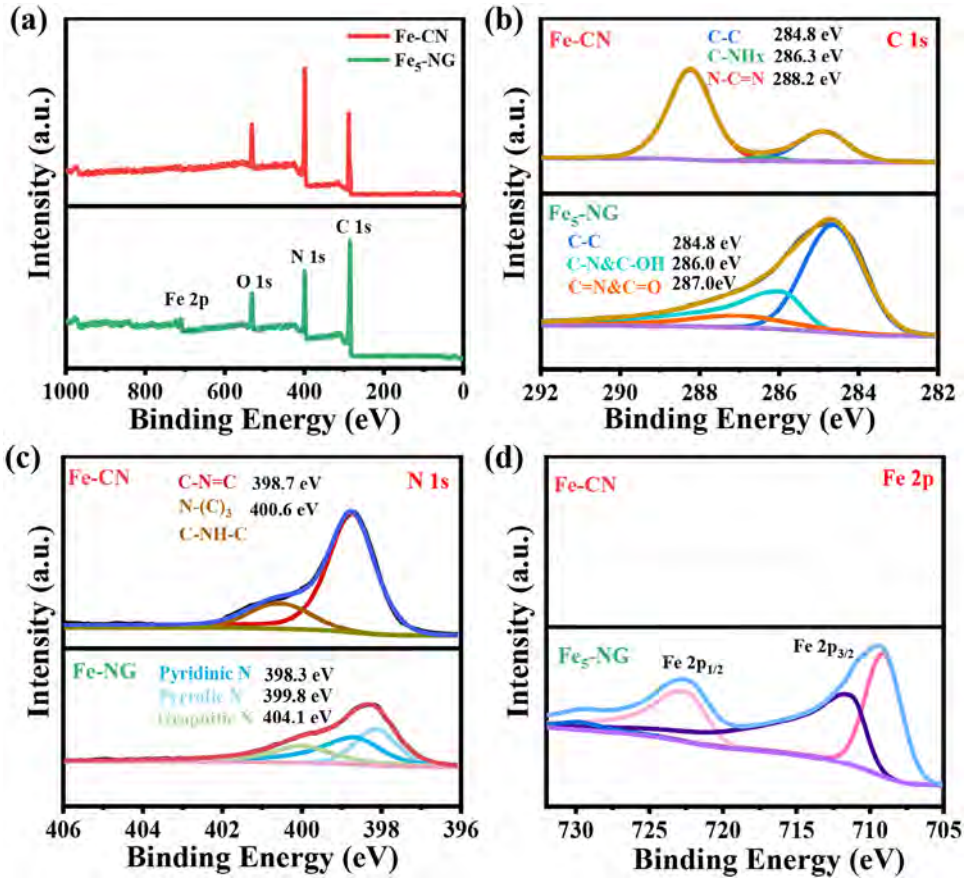

Figure 4. a) XPS survey spectra of Fe-CN and Fe_5-NG; High-resolution XPS spectra of b) C 1s, c) N 1s, and d) Fe 2*p* of Fe-CN and Fe_5-NG.

toward lower relative pressure and has a larger area, suggesting enhanced mesoporosity compared to Fe-CN. Figure 3a shows that the surface area of Fe_5-NG increases from 10.4 to 145.9 m^2/g compared to Fe-CN due to the gases produced by FePc during pyrolysis. In addition, Fe_5-NG has a richer pore structure and a wider pore size distribution than Fe-CN, with pore sizes ranging from 20–160 nm and mainly concentrated in the 20–40 nm range (Figure 3b).

The elemental composition and chemical states of Fe-CN and Fe_5-NG are determined by XPS. As shown in **Figure** 4a, both Fe-CN and Fe_5-NG contain C, O, N, and Fe. The C 1*s* spectrum of Fe-CN (Figure 4b) shows three peaks at 284.8, 286.3, and 288.2 eV, corresponding to C-C, C-NH_x, and N-C = N,[57] respectively. In comparison, the C 1*s* spectrum of Fe_5-NG exhibits peaks at 284.8 eV (C-C), 286.0 eV (C-N & C-OH), and 287.0 eV (C = N & C = O). The intensity of the peak at 284.8 eV (C-C) of Fe_5-NG is higher than that of Fe-CN because FePc makes Fe_5-NG more carbonized.[55] As shown in Figure 4c, the N 1*s* spectrum of Fe-CN exhibits two peaks: sp^2 hybridized N (C-N = C) in the triazine ring at 398.7 eV and tertiary N (N-$(C)_3$) & C-NH-C groups at 400.6 eV.[58,59] In contrast, the N 1*s* spectrum of Fe_5-NG shows three peaks corresponding to pyridine N at 398.0 eV, pyrrole N at 398.6 eV, and graphite N at 400.1 eV. Figure 4d shows that the Fe 2p peaks of the two samples are composed of Fe $2p_{3/2}$ (709.9 eV) and Fe $2p_{1/2}$ (722.5 eV). The peak intensity of Fe-CN is significantly weaker than that of Fe_5-NG due to the smaller Fe concentration in the former. The sharp Fe-$2p_{3/2}$ peak at 709.9 eV of Fe-NG corresponds to Fe-N, similar to Fe-phthalocyanine and Fe-N-C.[60]

3.2. Catalytic Activity

Figure 5a demonstrates the degradation efficacy of TC by Fex-NG modified with different doping ratios. $Fe_{0.5}$-NG/PMS achieves 84.8% TC degradation with minimal FePc, while efficiency peaks at 100% for Fe_5-NG/PMS as FePc content increases. As the FePc content is increased, the degradation efficiency of TC goes up, reaching 100% (Fe_5-NG/PMS). However, further increasing the FePc content decreases the TC degradation efficiency (Fe_{10}-NG/PMS) due to excessive accumulation of Fe, which hinders the activation of PMS.

Figure 5b shows the TC degradation results of the different samples. In the absence of PMS, Fe_5-NG alone degrades only 3.5% of TC, whereas in the absence of the catalyst, PMS alone degrades only 9.4% of TC as PMS is a potent oxidant. In the CN/PMS and Fe-CN/PMS systems, only 10.3% and 13.9% of TC are degraded, indicating that CN and Fe-CN have limited activity for PMS. The degradation efficiency of phthalocyanine-modified NG is 44.4% in the presence of PMS attributable to the larger surface area and porous framework of NG. In comparison, Fe_5-NG/PMS achieves 100% TC degradation within 12 min.

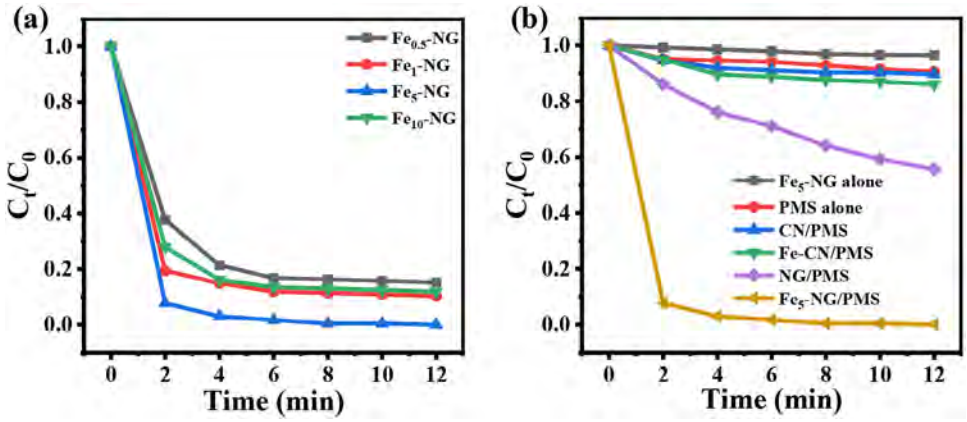

Figure 5. a) Decomposition profiles of TC for different ratios of the Fe_x-NG/PMS system and b) Comparison of the TC degradation curves of different systems (Experimental parameters: [cat.] = 0.1 g L^{-1}, [TC] = 25 mg L^{-1}, [PMS] = 0.5 mM, initial pH = 7).

Compared to the undoped NG, the significantly higher activation of Fe_5-NG to PMS is related to dispersed iron atoms. Under the same experimental conditions, we also evaluated the degradation efficiency of the Fe_5-NG/PMS system towards various pollutants (Figure S1, Supporting Information). The results demonstrate its exceptional degradation performance for RhB (Rhodamine B), MB (Methylene Blue), and TC, achieving over 90% removal within 2 min. This superior performance may be attributed to the abundant reactive sites provided by the amino groups it carries. The relatively poor degradation efficiency observed for 4-NP (4-Nitrophenol) (82% removal in 12 min) could potentially stem from the electron withdrawing nitro group reducing the electron density of the benzene ring, thereby decreasing its reactivity towards $^1O_2$ and resulting in lower degradation rates.

3.3. Influencing Factors

To design the optimal experimental parameters, the influence of the original pH, PMS dose, catalyst dose, and pollutant concentration on TC degradation is assessed. **Figure 6a** shows the effects of different TC concentrations on the removal efficiency of the Fe_5-NG /PMS system. TC concentrations below 25 mg L^{-1} yield 100% degradation within 12 min. With increasing TC concentration, the degradation efficiency decreases to 90.9% because the limited catalysts and PMS restrict the number of active species produced. At the same time, intermediates adsorb onto the catalyst surface to compete with TC for free radicals.[61] Therefore, a concentration of 25 mg L^{-1} is the standard TC concentration used in subsequent experiments.

Figure 6b illustrates the influence of dissimilar concentrations of Fe_5-NG on the degradation efficiency of TC. In the absence of Fe_5-NG, PMS alone cannot produce active species to degrade TC. By increasing the Fe_5-NG concentration from 0.01 to 0.1 g L^{-1}, the degradation efficiency increases from 88.3% to 100% due to more active sites for PMS activation. Further increasing the Fe_5-NG concentration to 0.15 g L^{-1} promotes the degradation rate only slightly, and the overall degradation efficiency remains at 100%, as observed at 0.1 g L^{-1}. Consequently, a concentration of 0.1 g L^{-1} is adopted for the Fe_5-NG concentration in our experiments.

Figure 6c shows the effects of different PMS concentrations. The TC degradation efficiency improves from 91.3% to 100% as the PMS concentration increases from 0.1 mM to 0.5 mM due to more active species. However, increasing the PMS concentration further to 0.7 mM reduces the efficiency because of the self-suspension of excess PMS and consumption of hydroxyl radicals.[63] Consequently, a PMS concentration of 0.5 mM is used in our experiments.

The original pH of the solution plays a pivotal role in the degradation process. The pH is changed using 0.1 mM H_2SO_4 and 0.1 mM NaOH. As shown in Figure 6d, the Fe_5-NG/PMS system removes 100% of TC under acidic and neutral conditions. However, at an alkaline pH of 9), the degradation rate decreases to 96.4% within 12 min. Under strong alkaline conditions (pH = 11), degradation by Fe_5-NG /PMS is inhibited because of Fe precipitation to form iron hydroxide.[55]

3.4. Stability and Reusability

Reproducibility and stability are key factors in the practical application of multiphase catalysts. Here, the effects of HCO–3, CO2- 3, Cl^-, PO3–4, and HA on TC degradation are examined (**Figure 7a**). In general, most anions have little effect on TC removal, showing >80% degradation. The small decrease stems from the depletion of active species by inorganic anions. PO3–4 has a greater influence on TC removal, with the degradation rate reduced to 61.8%. This is mainly due to the tetrahedral structure of PO3–4, which increases the competition for the surface functional groups and obstructs TC degradation on Fe_5-NG /PMS.[64]

The effects of different kinds of water (tap water and lake water) are determined to gauge the potential for practical applications. Figure 7b shows that the degradation efficiency of TC decreases slightly to 96.5% and 98.1% for tap water and lake water, confirming the good resistance to interferences in real water. The cycling stability of Fe_5-NG is investigated by five consecutive experiments (Figure 7c), and 100% removal is shown in the first three experiments. However, in the 4th and 5th experiments, the degradation efficiency decreases slightly to 97.3% and 87.7% respectively. Compared with Fe_5-NG, both Fe_{10}-NG and Fe_1-NG not only exhibited lower overall degradation rates, but also showed

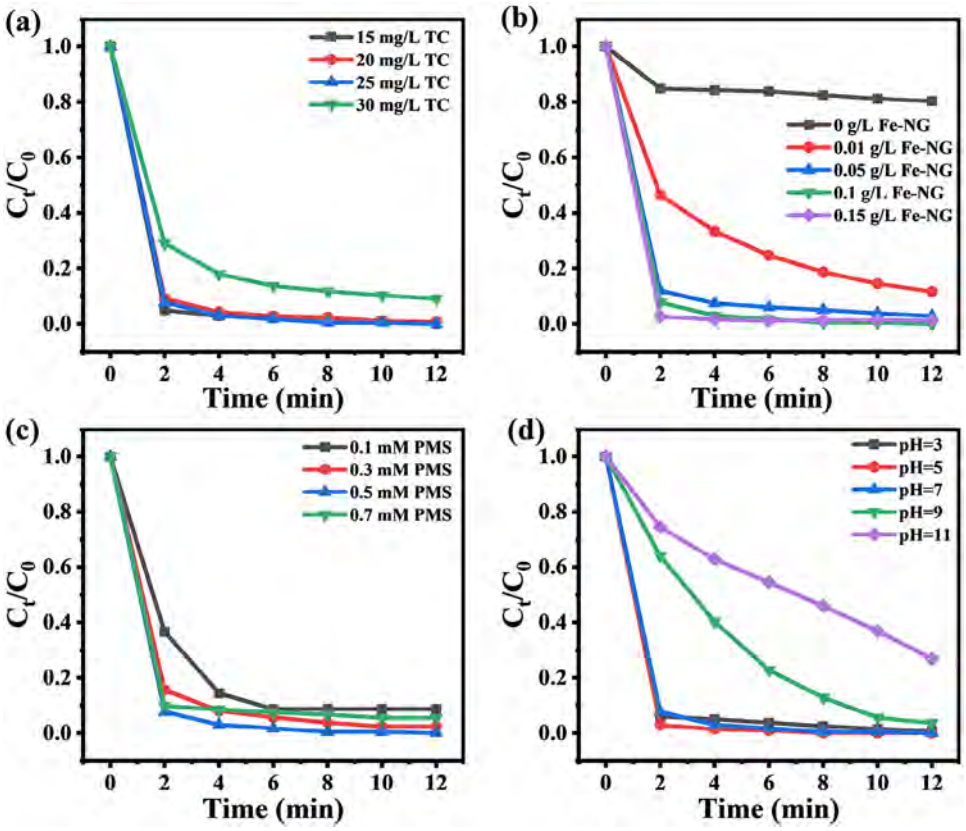

Figure 6. Effects of different factors in TC degradation: a) TC concentration, b) Fe_5-NG concentration, c) PMS concentration, and d) Initial pH.

more pronounced performance decrease after five cycles (Figure S2, Supporting Information). The decline in Fe_1-NG may be attributed to the coverage of active sites by contaminants, while the decrease in Fe_{10}-NG could result from metal leaching leading to the loss of active sites. The catalyst demonstrates significant superiority over comparable ones.[62] Hence, Fe_5-NG shows reasonable cycling stability.

Leaching of Fe species at different pH values is studied. Figure 7d shows that without PMS, Fe leaching is relatively constant at 0.15 mg/L in the pH range of 3–11. However, after adding PMS, Fe leaching increases primarily due to the redox reactions between Fe(II) and Fe(III).[49,65] The conversion from Fe(II) to Fe(III) is generally observed in the activation of PMS, and this valence change reduces the stability further leading to Fe leaching.

3.5. Mechanism of TC Degradation

To obtain a better understanding of the mechanism of TC degradation and identify the reactive species involved, radical scavenging experiments are conducted, as illustrated in **Figure** 8a. 5 mM BQ, 0.5 M TBA, 0.5 M MeOH, and 5 mM FFA are used to burst superoxide radicals ($^{\bullet}O–2$), hydroxyl radicals ($^{\bullet}OH$), sulphate radicals ($SO_4^{\bullet-}$) and singlet oxygen ($^1O_2$), respectively. As for $^{\bullet}OH$, both TBA and MeOH exhibit significant scavenging effects, with rate constants of k = 3.8–7.6 × 10^8 $M^{-1}s^{-1}$ and k = 8–10 × 10^8 $M^{-1}s^{-1}$, respectively. In contrast, with regard to $SO_4^{\bullet-}$, TBA shows a relatively minor scavenging effect (k = 4–9.1 × 10^5 $M^{-1}s^{-1}$), while MeOH exhibits a more pronounced effect (k = 0.9–1.3 × 10^7 $M^{-1}s^{-1}$). By comparing the scavenging effects of MeOH and TBA, the contribution of $SO_4^{\bullet-}$ can be evaluated. Additionally, TC degradation is inhibited by the addition of MeOH (82.4%) compared to the addition of TBA. The results confirm the crucial role of $SO_4^{\bullet-}$. The degradation efficiency decreases to 85.4% after $^{\bullet}O–2$ has been scavenged by BQ, indicating that $^{\bullet}O–2$ plays an important role in the Fe_5-NG/PMS system. Notably, FFA inhibits TC degradation appreciably, signifying that $^1O_2$ is the most important species in the system. Based on formulas SEq. 1 and SEq. 2, the contribution percentages of various reactive oxygen species were calculated. $^1O_2$ exhibited the highest contribution (40.7%), indicating its role as the predominant reactive species. The contribution values of $SO_4^{\bullet-}$ and $^{\bullet}O–2$ were comparable at 23.5% and 29.3% respectively, highlighting the importance of synergistic effects between free radicals. The $^{\bullet}OH$ showed a minimal contribution of only 6.8%, which may be attributed to the preferential orientation of Fe-N coordination bonds towards non-radical pathways.[66]

Fe-containing carbonaceous materials often activate PMS to produce high-valent iron species (Fe(IV) = O), so DMSO is used to verify the presence of Fe(IV) = O. DMSO can react with Fe(IV) = O to extract O and produce the corresponding sulfone ($DMSO_2$). Figure 8a shows that the addition of DMSO reduces the TC degradation efficiency to 77.1%, confirming that

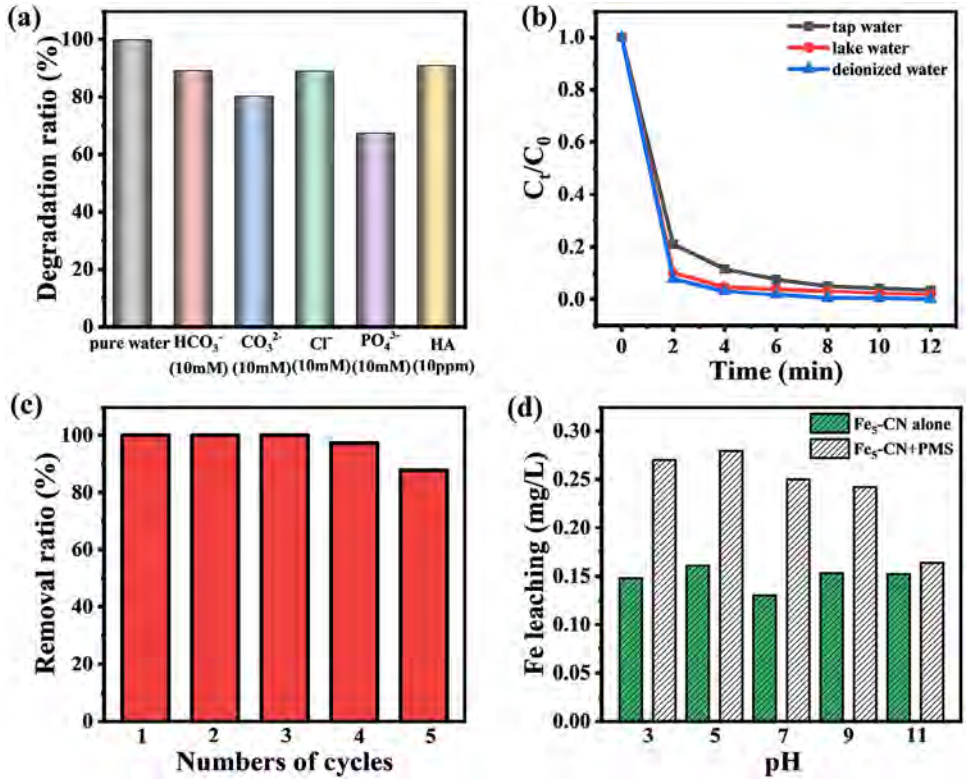

Figure 7. a) Effects of anions and humic acids on degradation; b) Degradation of TC in various water matrices using the Fe-NG/PMS system; c) Degradation of TC by Fe_5-NG/PMS for five cycles; d) Fe leaching for the various systems at different pH values.

Fe(IV) = O is oxidized selectively and serves as the main active species. Electron spin resonance (ESR) spectroscopy validates the presence of active species. Figure 8b–d shows that the signals of DMPO-$SO_4^{\bullet-}$, DMPO-$^{\bullet}$OH, DMPO-$^{\bullet}$O–2, and TEMP-$^1O_2$ adducts increase with reaction time, providing clues that $SO_4^{\bullet-}$, $^{\bullet}$OH, $^{\bullet}$O–2and $^1O_2$ are all present in the Fe_5-NG/PMS system.

The study indicates that electron transfer between materials and pollutants can accelerate reaction rates. To investigate the electron transfer characteristics of the Fe_5-NG system, electrochemical tests were conducted to analyze its i-t curve and EIS spectra. As shown in Figure S3a (Supporting Information), the current became more negative upon the addition of PMS and then stabilized, suggesting the system reached equilibrium. At 200 s, the introduction of TC caused a gradual increase in current, demonstrating that the synergistic effect between TC and PMS enhanced electron transfer. In Figure S3b (Supporting Information), the EIS spectra reveal that Fe_5-NG exhibits a smaller impedance radius, confirming its superior electron transfer capability. This enables electrons to rapidly activate PMS through active sites, thereby facilitating the degradation of TC.

In order to identify the main active sites in response to PMS activation, the changes in the surface structure of the reaction sequence Fe_5-NG are analyzed by XPS (**Figure 9**). The total N content decreases from 24.7 at% to 16.3 at% after the reaction. A significant decrease in pyridine N from 30.8 at% to 17.4 at% is observed after the reaction, but there are only moderate increases in pyrrole N (from 40.0 at% to 49.2 at%) and graphite N (from 27.2 at% to 33.4 at%), confirmed that pyridine N is the active nitrogen species in the activation of PMS. Nitrogen doping may produce a nonuniform arrangement of electrons, making the polarized carbon atoms around the dopant susceptible to reacting with negatively charged PMS to form sub-stable PMS with an internal electron rearrangement. Sub-stable PMS extracts electrons from the electron-rich N in the carbon network to form the active species to attack TC, and nitrogen-rich Fe_5-N provides abundant free electrons and a broad reaction platform.

Figure 9b shows that Fe(II)$2p_{3/2}$ and Fe(II)$2p_{1/2}$ in the Fe 2p spectrum of Fe_5-NG decrease from 32.3% and 23.7% to 24.5% and 20.8% after the reaction, respectively. Conversely, Fe(III)$2p_{3/2}$ and Fe(III)$2p_{1/2}$ increase from 39.8% and 4.2% to 46.0% and 8.7% after the reaction, respectively. This is because Fe(II) contributes electrons for PMS to produce active sulfate radicals and hydroxyl radicals Equations (2) and (3). PMS can also reduce Fe(III) in a higher valence state to Fe(II) in a lower valence state to form a redox cycle of Fe(III) and Fe(II) Equation (4). It has been reported that the abundance of free electrons in carbon materials may accelerate the redox cycle of Fe(III) and Fe(II) Equation (5).[67] Based on this, it can be concluded that prior to the reaction, pyridinic N stabilizes the dispersion of Fe in the material through Fe-N bonds. During PMS activation, pyridinic nitrogen provides electrons to facilitate the Fe(II)/Fe(III) redox cycling.[68,69] The loss of pyridinic N disrupts the stability of Fe-N coordination, which consequently leads to incomplete Fe(II) regeneration and performance degradation after four cycles.

$$HSO_5^- + e^- \rightarrow SO_4^{\cdot -} + OH^- \quad (1)$$

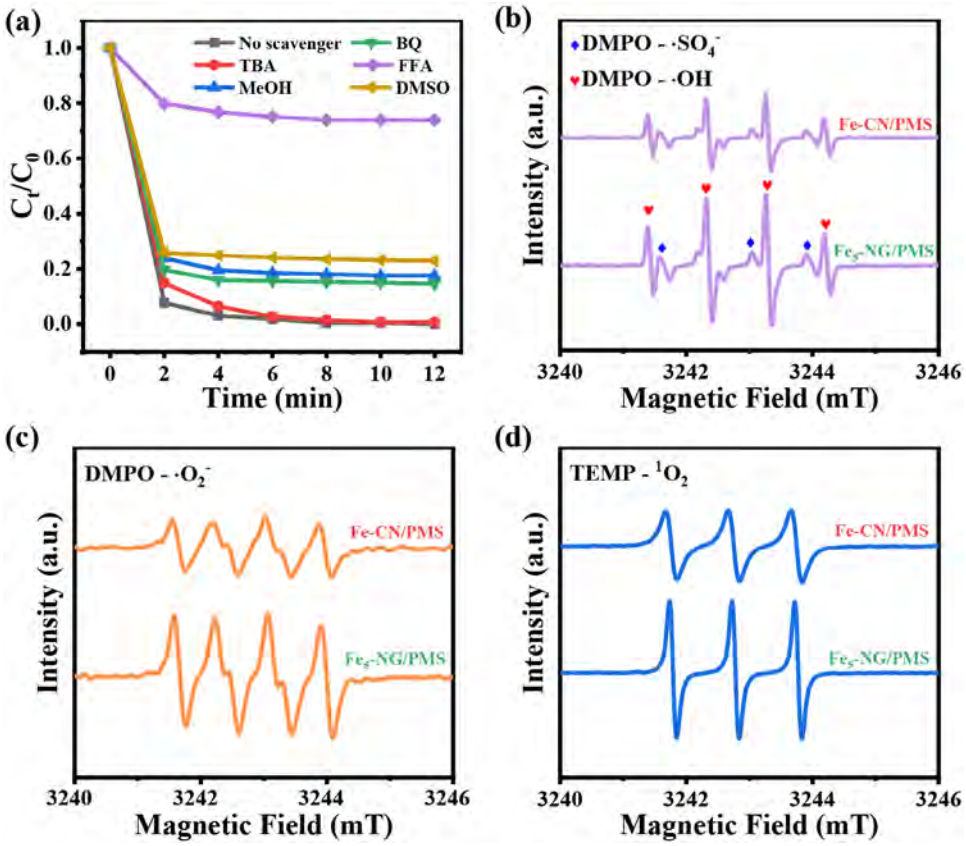

Figure 8. a) Effects of different radical scavengers on TC degradation for the Fe_5-NG/PMS system; b) ESR spectra of DMPO-•OH and DMPO-SO_4•−; c) ESR spectra of DMPO-•O–2; d) ESR spectra of TEMP-$^1O_2$ for the Fe_5-NG/PMS system.

$$Fe\,(II) + HSO_5^- \rightarrow Fe\,(III) + SO_4^{\cdot -} + OH^- \quad (2)$$

$$SO_4^{\cdot -} + OH^- \rightarrow OH + SO_4^{2-} \quad (3)$$

$$Fe\,(III) + HSO_5^- \rightarrow Fe\,(II) + SO_5^- + H^+ \quad (4)$$

$$Fe\,(III) + e^- \rightarrow Fe\,(II) \quad (5)$$

$$HSO_5^- + H_2O \rightarrow HSO_4^- + H_2O_2 \quad (6)$$

$$H_2O_2 \rightarrow 2 \cdot OH \quad (7)$$

$$\cdot OH + H_2O_2 \rightarrow HO_2^{\cdot} + H_2O \quad (8)$$

$$HO_2^{\cdot} \rightarrow H^+ + \cdot O_2^- \quad (9)$$

$$2 \cdot O_2^- + 2H_2O \rightarrow {}^1O_2 + H_2O_2 + 2OH^- \quad (10)$$

$$SO_5^{2-} + HSO_5^- \rightarrow SO_4^{2-} + HSO_4^- + {}^1O_2 \quad (11)$$

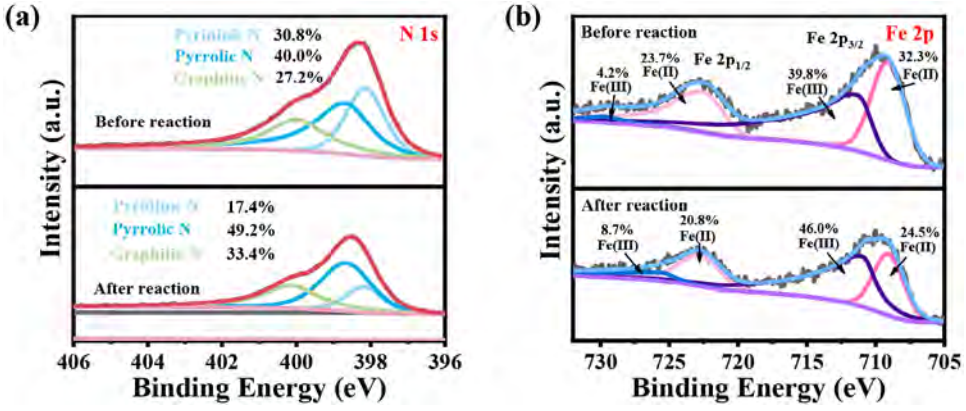

Figure 9. a) XPS N 1s spectra of pristine and used Fe_5-NG and b) Fe 2*p* spectra of fresh and used Fe_5-NG.

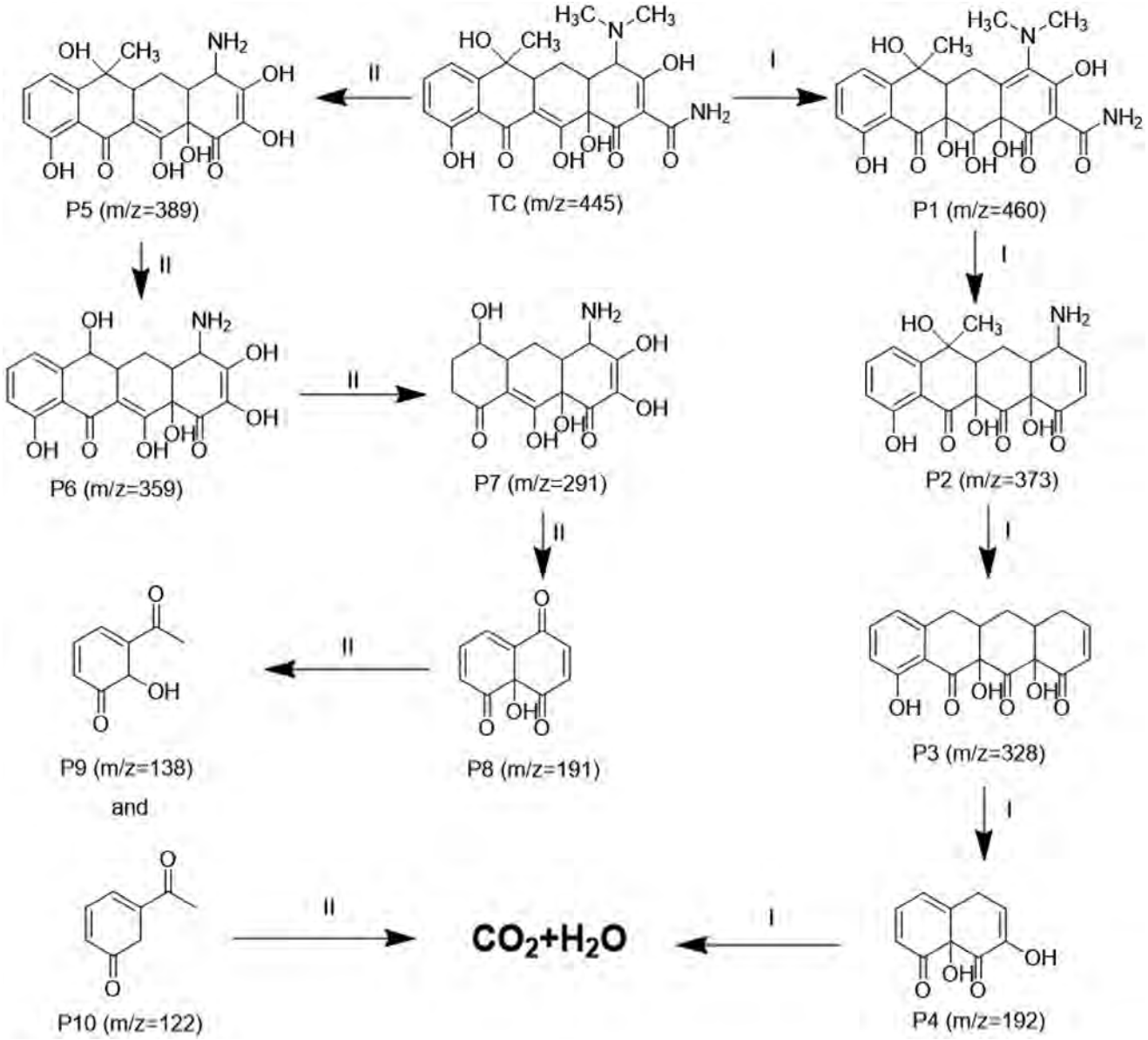

Figure 10. Two proposed TC degradation pathways for the Fe5-NG/PMS system.

$$Fe(II) + HSO_5^- \rightarrow Fe(II) - HSO_5^- \rightarrow Fe(IV) = O + SO_4^{2-} + 2H^+ \quad (12)$$

LC-MS is performed to identify the intermediate products during TC degradation. Based on the results, two possible pathways are proposed for the Fe_5-NG/PMS system (**Figure 10**). In pathway I, TC undergoes ketonization to form P1 (m/z = 460) through the attack of reactive species. Subsequently, the methyl nitrogen and amide groups on P1 are removed to yield P2 (m/z = 373). P2 then loses one molecule each of hydroxyl, methyl, and amino groups to form P3 (m/z = 328). P3 is progressively converted into a smaller intermediate P4 (m/z = 192). In degradation pathway II, TC loses the amide group, and two methyl groups attached to the nitrogen are attacked by active radicals to form P5 (m/z = 389). P5 then loses its methyl group to yield P6 (m/z = 359). P6 is further deprived of hydroxyl and amino groups, leading to progressive ring opening and the formation of P7 (m/z = 291), P8 (m/z = 191), P9 (m/z = 138), and P10 (m/z = 122). Finally, under the influence of active substances, these intermediates are gradually converted into CO_2 and H_2O.

Based on the above discussion, a mechanism for the TC degradation is proposed for the Fe_5-NG/PMS system in **Figure 11**. The degradation pathways can be divided into non-radical and free-radical ones, with the non-radical pathway being the predominant one. In the free-radical pathway, PMS generates $SO_4^{\cdot -}$ by extracting free electrons or reacting with Fe(II) Equations (1) and (2). $SO_4^{\cdot -}$ further generates $^{\cdot}OH$ Equation (3), while PMS can also be hydrolyzed to generate $^{\cdot}OH$ directly Equations (6) and (7). $^{\cdot}OH$ can generate $^{\cdot}O$–2 by Equations (8) and (9). In the non-radical pathway, $^1O_2$ is mainly derived from the reaction of $^{\cdot}O_2^-$ with H_2O Equation (10). The superior degradation

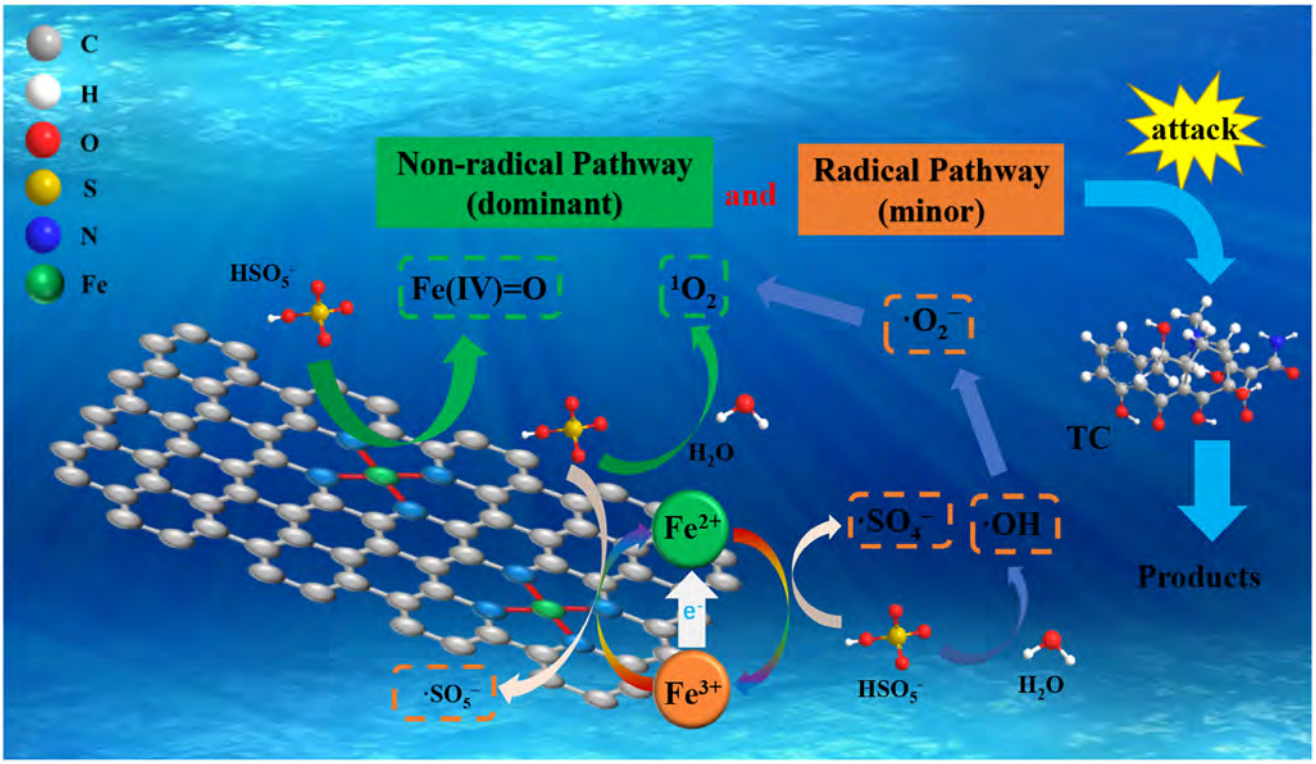

Figure 11. Possible mechanism of TC degradation by the Fe_5-NG/PMS system.

performance of Fe_5-NG stems from the synergistic effects of Fe sites and nitrogen species (pyridinic N and graphitic N) in activating PMS to generate free radicals. Specifically, pyridinic nitrogen stabilizes highly dispersed Fe atoms through Fe—N bonds. The electron-rich nature of pyridinic nitrogen enhances material adsorption of PMS, improves electron conduction, and accelerates electron transfer to both PMS and Fe(III), thereby sustaining the Fe(II)/Fe(III) redox cycle. Concurrently, graphitic nitrogen and Fe-N configurations promote PMS decomposition to generate $^1O_2$ Equation (11).[51] In addition, high valent iron species (Fe(IV) = O) play an important role in the Fe_5-NG/PMS system Equation (12). Ultimately, under the synergistic effect of the Fe_5-NG/PMS system, these free radicals and non-radical species collectively formed an integrated reaction network, mineralizing TC into H_2O and CO_2.

4. Conclusions

Fe_5-NG porous carbon catalysts are fabricated by a one-step calcination method with iron phthalocyanine as the precursor. The products exhibit a unique porous structure and morphology. The optimal Fe_5-NG/PMS system shows remarkable degradation efficiency by achieving 100% tetracycline degradation within 12 min. The key factor is the synergistic interaction between Fe and N, particularly through the formation of Fe—N bonds. The Fe—N bonds drive PMS activation, enabling efficient generation of $SO_4^{\cdot-}$ and $^1O_2$ for TC degradation. Overall, Fe_5-NG shows great potential in environmental remediation, especially the degradation of common pollutants such as tetracycline. The critical role of Fe-N bonds in the superior catalytic activity is confirmed.

Supporting Information

Supporting Information is available from the Wiley Online Library or from the author.

Acknowledgements

This study was financially supported by the National Natural Science Foundation of China (22108110, 22108106, 22308300), Jiangsu Engineering Laboratory of New Materials for Sewage Treatment and Recycling (SDGC2304). Natural Science Foundation of Jiangsu Province (BK20220598), City University of Hong Kong Donation Research Grants (DON-RMG No. 9229021 and 9220061), and Key Laboratory of Electrochemical Energy Storage and Energy Conversion of Hainan Province (No. KFKT2024005).

Conflict of Interest

The authors declare no conflict of interest.

Data Availability Statement

The data that support the findings of this study are available from the corresponding author upon reasonable request.

Keywords

Iron phthalocyanine, non-free radicals, peroxymonosulfate activation, tetracycline degradation

Received: February 24, 2025
Revised: April 18, 2025
Published online: June 4, 2025

[1] R. Daghrir, P. Drogui, *Environ. Chem. Lett.* **2013**, *11*, 209.
[2] L. Xiao, J. Liu, J. Ge, *Agric. Water Manag.* **2021**, *243*, 106417.
[3] L.Cui, P. Wang, H. Che, X. Gao, J. Chen, B. Liu, Y. Ao, *Water Res.* **2023**, *244*, 120514.
[4] J. Yang, L. Jing, X. Zhu, W. Zhang, J. Deng, Y. She, K. Nie, Y. Wei, H. Li, H. Xu, *Appl. Catal., B* **2023**, *320*, 122005.
[5] J. Scaria, A. Gopinath, N. Ranjith, V. Ravindran, S. Ummar, P. Nidheesh, M. S. Kumar, *J. Clean. Prod.* **2022**, *350*, 131319.
[6] J. Niu, R. Yuan, H. Chen, B. Zhou, S. Luo, *Environ. Res.* **2024**, *262*, 119889.
[7] A. James, J. D. Rodney, S. Joshi, U. Dalimba, B. C. Kim, N. Udayashankar, *Chem. Eng. J.* **2024**, *481*, 148466.
[8] G. Liu, Z. Liu, Y. Sun, M. Sun, J. Duan, Y. Tian, D. Du, M. Li, *Foods* **2024**, *13*, 3192.
[9] P. R. Gogate, *Recent Adv.* **2020**, *378*, 71.
[10] B. Wang, H. Chen, W. Zhang, H. Liu, Z. Zheng, F. Huang, J. Liu, G. Liu, X. Yan, Y. X. Weng, *Adv. Mater.* **2024**, *36*, 2312676.
[11] M. Kohantorabi, G. Moussavi, S. Giannakis, *Chem. Eng. J.* **2021**, *411*, 127957.
[12] P.-M. Hannula, A. Peltonen, J. Aromaa, D. Janas, M. Lundström, B. P. Wilson, K. Koziol, O. Forsén, *Carbon* **2016**, *107*, 281.
[13] B. Wang, J. Zhao, H. Chen, Y.-X. Weng, H. Tang, Z. Chen, W. Zhu, Y. She, J. Xia, H. Li, *Appl. Catal. B.* **2021**, *293*, 120182.
[14] G. Song, F. Qin, J. Yu, L. Tang, Y. Pang, C. Zhang, J. Wang, L. Deng, *J. Hazard. Mater.* **2022**, *424*, 127663.
[15] J. Liu, H. Xu, Y. Xu, Y. Song, J. Lian, Y. Zhao, L. Wang, L. Huang, H. Ji, H. Li, *Appl. Catal. B.* **2017**, *207*, 429.
[16] W. Li, X. Hu, Q. Li, Y. Shi, X. Zhai, Y. Xu, Z. Li, X. Huang, X. Wang, J. Shi, *Food Chem.* **2020**, *320*, 126623.
[17] W. Yang, C. Liu, B. Zhang, C. Wu, Y. Cao, W. Huang, W. Xu, *Food Anal. Methods* **2024**, *17*, 1689.
[18] S. Wei, Y. Sun, Y.-Z. Qiu, A. Li, C.-Y. Chiang, H. Xiao, J. Qian, Y. Li, *Nat. Commun.* **2023**, *14*, 7549.
[19] M. Qian, F. Xu, H. Bi, T. Lin, F. Huang, *Carbon* **2017**, *112*, 47.
[20] S. Qiu, X. Wu, L. Xiao, X. Ai, H. Yang, Y. Cao, *ACS Appl. Mater. Interfaces.* **2016**, *8*, 1337.
[21] X. Zhao, P. Gao, B. Shen, X. Wang, T. Yue, Z. Han, *Renew. Sust. Energ. Rev.* **2023**, *188*, 113808.
[22] S. Shao, T. Sun, X. Li, Y. Wang, L. Ma, Z. Liu, S. Wu, *Ind. Crops Prod.* **2024**, *218*, 118963.
[23] B. Wang, W. Zhang, G. Liu, H. Chen, Y. X. Weng, H. Li, P. K. Chu, J. Xia, *Adv. Funct. Mater.* **2022**, *32*, 2202885.
[24] M.-X. Wang, Z.-Y. Guo, Z.-H. Huang, F.-Y. Kang, *New Carbon Mater.* **2016**, *31*, 277.
[25] X. Wei, M. Naraghi, H. D. Espinosa, *ACS Nano* **2012**, *6*, 2333.
[26] L. Wang, X. Zhu, Y. Guan, J. Zhang, F. Ai, W. Zhang, Y. Xiang, S. Vijayan, G. Li, Y. Huang, *Energy Stor. Mater.* **2018**, *11*, 191.
[27] D.-Q. Li, Y.-J. Meng, J. Li, Y.-J. Song, F. Xu, *Carbohydr. Polym.* **2022**, *288*, 119400.
[28] R. Catalão, F. Maldonado-Hódar, A. Fernandes, C. Henriques, M. Ribeiro, *Appl. Catal. B.* **2009**, *88*, 135.
[29] M. Zhou, C. Yang, G. Chan, *Adv. Energy Mater.* **2014**, *4*, 1400840.
[30] S. Zhu, Q. Ruan, X. Zhu, D. Li, B. Wang, C. Huang, L. Liu, F. Xiong, J. Yi, Y. Song, *J. Colloid Interface Sci.* **2024**, *664*, 736.
[31] Y. Wen, J. Chen, X. Gao, W. Liu, H. Che, B. Liu, Y. Ao, *Nano Energy* **2023**, *107*, 108173.
[32] Q. Zhang, T. Wu, H. Che, C. Tang, B. Liu, Y. Ao, *Surf. Interfaces* **2024**, *47*, 104205.
[33] Q. Ye, M. Li, T. Xiao, S. Hou, Y. Deng, J. Luo, X. Tian, *Int. J. Hydrogen Energy.* **2024**, *49*, 1014.
[34] X. Cheng, Z. Shen, L. Jiao, L. Yang, X. Wang, Q. Wu, Z. Hu, *J. Energy Chem.* **2021**, *3*, 100066.
[35] D. Qiu, B. Zhang, T. Zhang, T. Shen, Z. Zhao, Y. Hou, *ACS Nano* **2022**, *16*, 21443.
[36] H. Tan, Y. Zhao, W. Xia, J. Zhao, X. Xu, K. Wood, Y. Sugahara, Y. Yamauchi, J. Tang, *Chem. Mater.* **2020**, *32*, 4248.
[37] R. Zheng, Q. Meng, H. Zhang, T. Li, D. Yang, L. Zhang, X. Jia, C. Liu, J. Zhu, X. Duan, *J. Energy Chem.* **2024**, *90*, 7.
[38] J. Guo, B. Li, Q. Zhang, Q. Liu, Z. Wang, Y. Zhao, J. Shui, Z. Xiang, *Adv. Sci.* **2021**, *8*, 2002249.
[39] X. Bai, P. Hu, A. Li, Y. Zhang, A. Li, G. Zhang, Y. Xue, T. Jiang, Z. Wang, H. Cui, *Nature* **2024**, *634*, 80.
[40] A. Wang, R. Fan, X. Pi, Y. Zhou, G. Chen, W. Chen, Y. Yang, *ACS Appl. Mater. Interfaces* **2018**, *10*, 37407.
[41] A. Kumar, V. K. Vashistha, D. K. Das, *Coord. Chem. Rev.* **2021**, *431*, 213678.
[42] L. Liu, W. Xiao, J. Mao, H. Zhang, Y. Jiang, H. Zhou, K. Yang, H. Gao, *Chin. Chem. Lett.* **2018**, *29*, 183.
[43] H. Gu, Y. Dong, R. Lv, X. Huang, Q. Chen, *Food Quality Safety* **2022**, *6*, fyac046.
[44] Z. Zhang, M. Dou, J. Ji, F. Wang, *Nano Energy* **2017**, *34*, 338.
[45] D. Xu, X. Li, T. Zheng, R. Zhao, P. Zhang, K. Li, Z. Li, L. Zheng, X. Zuo, *Nanoscale Adv.* **2022**, *4*, 2171.
[46] F. Wu, H. Huang, T. Xu, W. Lu, N. Li, W. Chen, *Appl. Catal. B.* **2017**, *218*, 230.
[47] Y. Wang, M. Wang, Z. Zhang, Q. Wang, Z. Jiang, M. Lucero, X. Zhang, X. Li, M. Gu, Z. Feng, *ACS Catal.* **2019**, *9*, 6252.
[48] B. Mukherjee, *J. Electrochem. Soc.* **2020**, *16*, 116501.
[49] J. Xu, Q. Zhang, X. Gao, P. Wang, H. Che, C. Tang, Y. Ao, *Angew. Chem., Int. Ed.* **2023**, *135*, 202307018.
[50] D. Zhang, Y. Guo, Z. Zhao, *Appl. Catal. B.* **2018**, *226*, 1.
[51] S. Hou, H. Hu, Q. Fu, T. Xiao, J.-Q. Xie, S.-H. Chan, M. He, B. Miao, L. Zhang, *Sep. Purif. Technol.* **2024**, *333*, 125980.
[52] C. Liu, H. Huang, W. Cui, F. Dong, Y. Zhang, *Appl. Catal. B.* **2018**, *230*, 115.
[53] J. Wang, B. Gao, M. Dou, X. Huang, Z. Ma, *Environ. Res.* **2020**, *184*, 109339.
[54] S. Shenoy, C. Chuaicham, K. Sekar, K. Sasaki, *Environ. Chem. Lett.* **2024**, *23*, 33.
[55] H. Li, J. Qian, B. Pan, *Chem. Eng. J.* **2021**, *403*, 126395.
[56] J. Hamonnet, M. S. Bennington, B. Johannessen, J. Hamilton, P. A. Brooksby, S. Brooker, V. Golovko, A. T. Marshall, *ACS Catal.* **2022**, *12*, 14571.
[57] H. Sun, F. Guo, J. Pan, W. Huang, K. Wang, W. Shi, *Chem. Eng. J.* **2021**, *406*, 126844.
[58] F. Pan, Z. Cao, Q. Zhao, H. Liang, J. Zhang, *J. Power Sources.* **2014**, *272*, 8.
[59] H. Li, C. Shan, B. Pan, *Environ. Sci. Technol.* **2018**, *52*, 2197.
[60] F. Liu, N. Yan, G. Zhu, Z. Liu, S. Ma, G. Xiang, S. Wang, X. Liu, W. Wang, *New J. Chem.* **2021**, *45*, 13004.
[61] J. Li, Y. Liu, X. Ren, W. Dong, H. Chen, T. Cai, W. Zeng, W. Li, L. Tang, *J. Colloid Interface Sci.* **2021**, *599*, 631.
[62] Y. Tao, T. Xiao, Q. Fu, B. Miao, S. Hou, G. Peng, Y. Xiong, M. Tang, *RSC Adv.* **2025**, *15*, 7307.
[63] T. Zhang, Y. Liu, Y. Rao, X. Li, D. Yuan, S. Tang, Q. Zhao, *Chem. Eng. J.* **2020**, *384*, 123350.
[64] R. Tang, D. Gong, Y. Deng, S. Xiong, J. Zheng, L. Li, Z. Zhou, L. Su, J. Zhao, *J. Hazard. Mater.* **2022**, *423*, 126944.
[65] Z. Wu, J. Shen, W. Li, J. Li, D. Xia, D. Xu, S. Zhang, Y. Zhu, *Appl. Catal. B.* **2023**, *330*, 122642.

[66] S. Wei, Y. Sun, Y.-Z. Qiu, A. Li, C.-Y. Chiang, H. Xiao, J. Qian, Y. Li, *Nat. Commun.* **2023**, *14*, 7549.
[67] L. Chen, Y. Huang, M. Zhou, K. Xing, L. Rao, W. Lv, Y. Yao, *Chem. Eng. J.* **2021**, *404*, 126537.
[68] Y. Xiong, H. Li, C. Liu, L. Zheng, C. Liu, J. O. Wang, S. Liu, Y. Han, L. Gu, J. Qian, *Adv. Mater.* **2022**, *34*, 2110653.
[69] B. Wang, H. Chen, F. Huang, J. Liu, G. Liu, Y.-X. Weng, Y. She, X. Zhu, H. Li, J. Xia, P. K. Chu, *Appl. Catal., B* **2025**, *374*, 125394.

Supporting information

Degradation of tetracycline by Fe-N-coordinated porous carbon activated PMS: High dispersibility and stability

Shenghui Wang[a], Yanhua Song[a*], Yansong Wu[a], Bin Wang[b], Xue Gao[c], Xingwang Zhu[d], Jinyuan Liu[b,c*], Paul K. Chu[b*]

[a] *School of Environmental and Chemical Engineering, Jiangsu University of Science and Technology, Zhenjiang, Jiangsu 212003, P. R. China*

[b] *Department of Physics, Department of Materials Science and Engineering, and Department of Biomedical Engineering, City University of Hong Kong, Tat Chee Avenue, Kowloon, Hong Kong, China*

[c] *Institute for Energy Research, School of the Environment and Safety Engineering, Jiangsu University, Zhenjiang, Jiangsu 212013, P. R. China*

[d] *Institute of Technology for Carbon Neutralization, College of Environmental Science and Engineering, Yangzhou University, Yangzhou 225009, China*

***Corresponding authors**: songyh@just.edu.cn (Y.H. Song); jyliu@ujs.edu.cn (J.Y. Liu); paul.chu@cityu.edu.hk (P.K. Chu)*

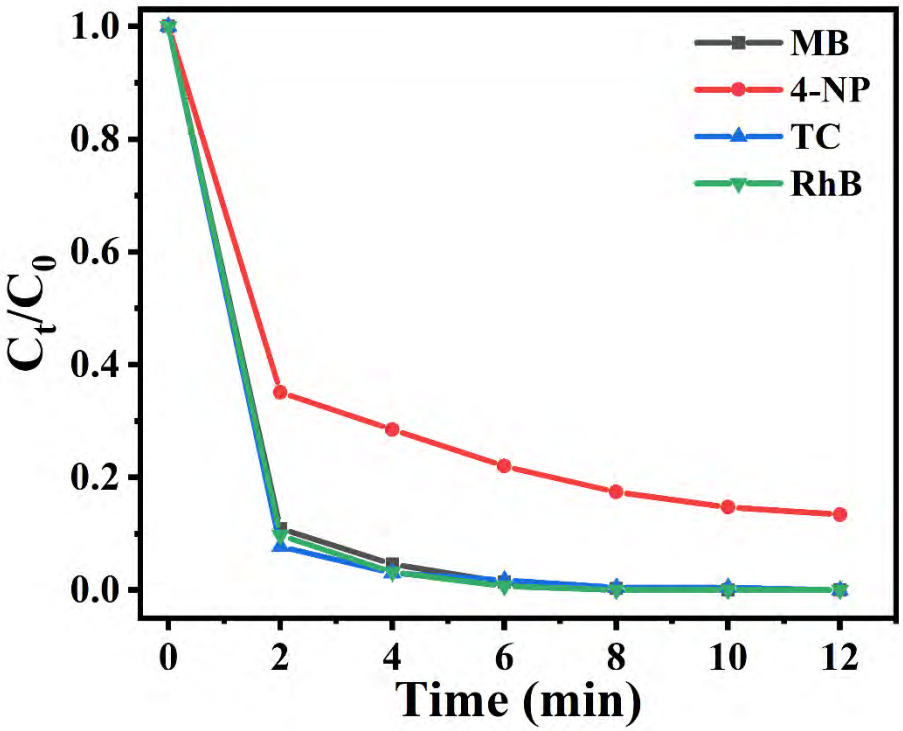

Fig.S1. Degradation effects of different contaminants.

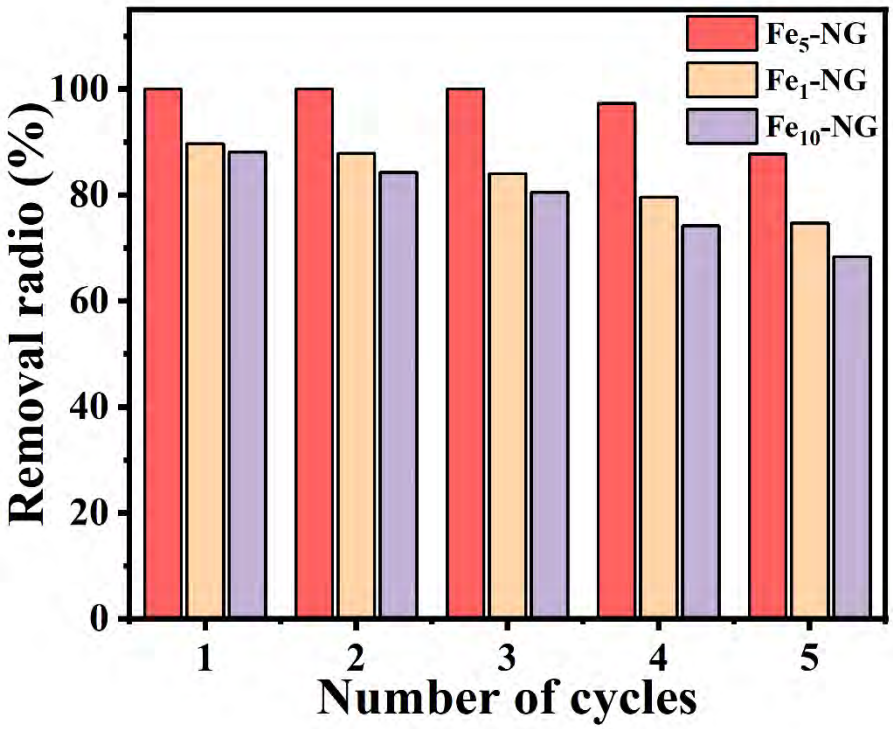

Fig.S2 Degradation of TC by Fe$_X$-NG/PMS (x = 1, 5, and 10) for five cycles

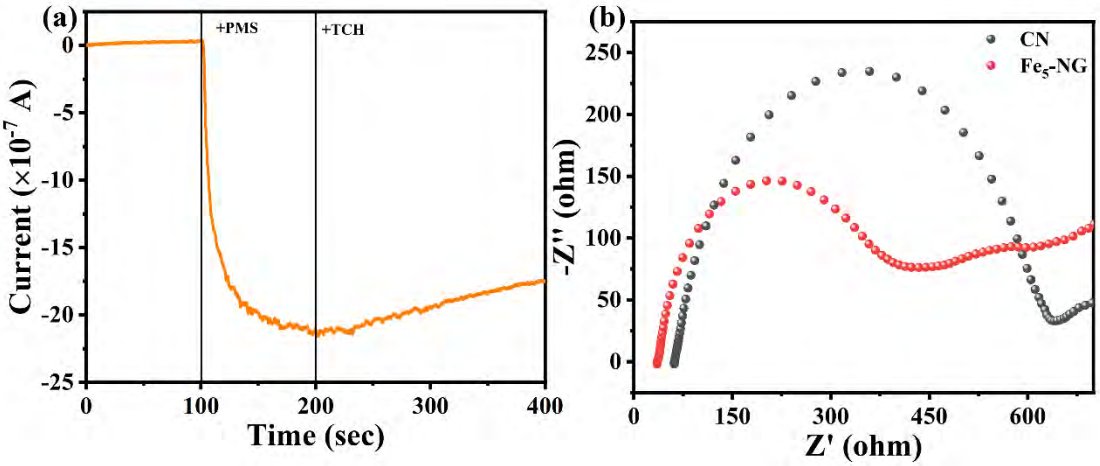

Fig. S3 (a) i-t curves obtained at 0.0 V vs. Ag/AgCl with Fe_5-NG; (b) EIS spectra of CN and Fe_5-NG loaded on the FTO glass electrodes.

$$\ln(C_t/C_0) = -K_{scavenger} \times t \quad \text{(S1)}$$

$$R_i = K_i/K_{obs} = \frac{K_{obs}-K_{scavenger}}{K_{obs}} \quad \text{(S2)}$$